



ISTITUTO NAZIONALE DI RICERCA METROLOGICA Repository Istituzionale

Verwey transition temperature distribution in magnetic nanocomposites containing polydisperse magnetite nanoparticles

This is the author's accepted version of the contribution published as:

Original

Verwey transition temperature distribution in magnetic nanocomposites containing polydisperse magnetite nanoparticles / Barrera, G.; Tiberto, P.; Sciancalepore, C.; Messori, M.; Bondioli, F.; Allia, P.. - In: JOURNAL OF MATERIALS SCIENCE. - ISSN 0022-2461. - 54:11(2019), pp. 8346-8360. [10.1007/s10853-019-03510-y]

Availability:

This version is available at: 11696/65888 since: 2021-02-09T17:45:33Z

Publisher:

Kluwer Academic Publishers

Published

DOI:10.1007/s10853-019-03510-y

Terms of use:

This article is made available under terms and conditions as specified in the corresponding bibliographic description in the repository

Publisher copyright

SPRINGER

Copyright © Springer. The final publication is available at link.springer.com

(Article begins on next page)

Verwey Transition Temperature Distribution in Magnetic Nanocomposites Containing Polydisperse Magnetite Nanoparticles

G. Barrera¹, P. Tiberto¹, C. Sciancalepore², M. Messori³, F. Bondioli^{2,4}, P. Allia^{4,*}

¹INRiM, Nanoscience and Materials, Strada delle Cacce 91, 10135 Torino Italy

²INSTM, National Interuniversity Consortium of Materials Science and Technology (Research Unit of Parma), Via Giusti 9, 50121 Florence, Italy

³University of Modena and Reggio, Department of Engineering “Enzo Ferrari”, Via Vivarelli 10 41125 Modena, Italy

⁴Politecnico di Torino, DISAT, Corso Duca degli Abruzzi 24, 10129 Torino, Italy

*Corresponding author at: Politecnico di Torino, DISAT, corso Duca degli Abruzzi 24, 10129 Torino Italy. E-mail address: paolo.allia@formerfaculty.polito.it

ORCID identifiers:

G. BARRERA: 0000-0002-3174-8092

P. TIBERTO: 0000-0002-5432-1788

C. SCIANCALEPORE: 0000-0002-8182-6618

M. MESSORI: 0000-0003-3598-4241

F. BONDIOLI: 0000-0002-4507-3831

P. ALLIA: 0000-0002-9132-1701

Abstract

Polymeric nanocomposites containing Fe_3O_4 nanoparticles were prepared through a chemical route under different precursor-to-solvent ratios and were submitted to structural and morphologic characterization. The embedded nanoparticles, containing pure magnetite and characterized by considerable polydispersity, are rather homogeneously dispersed in the matrix. The magnetic properties of two representative samples were analyzed in detail between $T = 5$ K and room temperature. Magnetic effects clearly associated to the Verwey monoclinic to cubic transition with transition temperatures distributed in the interval 95-120 K were put in evidence. On heating through this region, the coercive field and the maximum susceptibility of hysteresis loops display marked downward/upward steps, respectively, while the high-field magnetization is not affected at all; a comparable upward step is measured in the FC/ZFC curves. Reporting the maximum susceptibility as a function of the reciprocal of the coercive field in the interval from $T = 95$ K to $T = 120$ K, and using the predictions for single-domain nanoparticles with randomly distributed axes of uniaxial and cubic anisotropy (the former/latter case being applicable below/above the Verwey transition, respectively), the evolution of the transformed cubic-anisotropy fraction upon heating has been studied, and the distribution of Verwey transition temperatures related to the sample polydispersity has been accurately determined. The low-temperature value of the uniaxial anisotropy constant is obtained from coercive field measurements and found to be comparable to, albeit slightly higher than the corresponding quantity measured in bulk crystalline magnetite.

Keywords

Magnetite nanoparticles; magnetic nanocomposites; Verwey transition; magnetization process

1. Introduction

The Verwey transition, a well-known [1], still debated [1, 2] effect occurring in bulk magnetite near 125 K is revealed by a dramatic change of the electronic transport properties and by a corresponding change of magnetic properties such as magnetic anisotropy [1] and magnetostriction [3].

The recent years have witnessed a remarkable surge of research on sub-micrometric magnetite; in particular, Fe_3O_4 nanoparticles and related nanocomposites/nanocomplexes have attracted considerable attention owing to the combination of efficient preparation techniques [4–8], low toxicity [9] and ever increasing potential of applications in strategic fields such as sensors, **Information and Communication Technologies (ICTs)**, environment and biomedicine [8, 10–16].

As for all magnetic nanosystems, the magnetic properties of Fe_3O_4 nanoparticles are strongly affected by size effects; the measured differences from the bulk material are often ascribed to surface effects: for

instance, increasing the surface-to-volume ratio typically results in a reduction of the room-temperature saturation magnetization [17, 18] and an enhancement of magnetic anisotropy [19, 20] with respect to their bulk values.

In sharp contrast, the Verwey transition in magnetite particles appears as being rather elusive an effect. In fact, a number of sometimes contradictory results have been reported in the recent literature, including strong reduction [21–24] or even complete disappearance [25, 26] of the Verwey transition temperature T_V in small particles. A comprehensive study of the effect of nanoparticle size on T_V has been performed on nanocrystals grown around 5-nm seeds through seed-mediated nanocrystal growth [27]. In that case, the Verwey transition was found to be size-independent down to 20 nm with a progressive reduction of the transition temperature from 20 to 8 nm before suddenly disappearing below 6 nm.

However, size is not the only parameter influencing the value of T_V . The observation of the Verwey transition is related also to details of the nanoparticle preparation process, such as the presence of a magnetic field [26]. The particle shape plays an important role on the Verwey transition in ultrasmall nanoparticles [28]. As recently pointed out [29], the quality of magnetite (both structural and chemical) plays a most important role in determining the existence of the Verwey transition. In fact, a significant reduction of T_V has been measured in macroscopic magnetite single crystals as a function of increasing off-stoichiometry status [29]. The observation of T_V in nanometer-sized magnetite has been recently proven to be connected to the high quality of the sample [27, 30].

In this paper, a study based on structural, morphologic and magnetic data is conducted on a set of nanocomposites containing different amounts of polydisperse magnetite nanoparticles with sizes in the 5–70 nm range. The magnetic behavior of representative nanocomposite samples above and below the Verwey transition is explained making use of morphologic data; the changes in magnetic properties occurring at the Verwey transition are described in some detail. The ensuing analysis indicates that in this class of composites a continuous distribution of T_V values exists, suggesting that the embedded nanoparticles undergo the Verwey transition at different temperatures.

2. Experimental

2.1 Materials and Methods

All chemicals were high-purity grade and were used as received without any further purification. Bisphenol A diglycidyl ether (DGEBA, Dow D.E.R.[™] 332 with an epoxide equivalent weight of 172–176), diethylenetriamine (DETA) and acetone (AcO) were purchased by Sigma Aldrich (Milan, Italy). Acetylacetone (AcAcH), Iron(III)-chloride hexahydrate ($\text{FeCl}_3 \cdot 6\text{H}_2\text{O}$) and sodium acetate (NaOAc) were purchased from Carlo Erba (Milan, Italy).

2.2 Magnetite synthesis

The magnetite precursor, iron(III)-acetylacetonate ($\text{Fe}(\text{AcAc})_3$), was synthesized starting from $\text{FeCl}_3 \cdot 6\text{H}_2\text{O}$ and NaOAc , as described in Messori et al. [31]. According to **Non-Hydrolytic Sol-Gel (NHSG)** route, designed by Niederberger et al. [32] and already successfully used in the magnetic nanoparticles synthesis with alcohol solvents [18, 33, 34], in a 100 mL Schlenk tube 1.00 g (2.83 mmol) ($\text{Fe}(\text{AcAc})_3$) was dissolved in different amounts of DETA, in order to evaluate the effect of the precursor-to-solvent ratio on the powder properties. The precursor-to-solvent ratio was varied in the molar range 0.1-0.9 composition details in Table 1.

Powder Code	$\text{Fe}(\text{AcAc})_3$ (g)	DETA (g)	$\text{Fe}(\text{AcAc})_3$ (mol)	DETA (mol)	Ratio $\text{Fe}(\text{AcAc})_3/\text{DETA}$ (mol/mol)	Ratio $\text{Fe}(\text{AcAc})_3/-(\text{N})\text{H}$ (mol/mol)
Mag-DETA_1	1	2.6	0.0028	0.025	0.11	0.02
Mag-DETA_2	1	1.3	0.0028	0.013	0.22	0.04
Mag-DETA_4	1	0.7	0.0028	0.006	0.44	0.09
Mag-DETA_8	1	0.3	0.0028	0.0032	0.88	0.18

Table 1: Composition of the NHSG reaction batches

The reaction was left stirring at room temperature for 15 min and then heated to 200°C in an oil bath for 48 h.

After reaction, a stable suspension was obtained. To better characterize the inorganic phase, the obtained powders were re-dispersed in AcO with an ultrasonic bath and centrifuged at 4000 rpm for 60 min; the powders were washed, centrifuged until the obtainment of a colorless liquid phase and finally dried under reduced pressure.

2.3 Powder characterization

X-ray powder diffraction (XRPD) data for qualitative and quantitative phase analysis were collected using a Bragg–Brentano θ -2 θ diffractometer (X'Pert PRO PANalytical, Netherlands) equipped with a gas proportional detector.

Nanoparticle size and morphology were examined by transmission electron microscopy (TEM) investigation, performed on a Tecnai 12 Gspirit electron microscope (FEI Company, USA), using an accelerating voltage of 120 kV and LaB_6 as electron source.

Experimental histograms of nanoparticle size distribution were obtained by TEM image analysis. The grain size was approximated by the equivalent circular diameter (or Heywood diameter, E.C.D), representing the diameter of the circle having the area equivalent to the nanoparticle area [35]. The resulted histograms were fitted by the log-normal distribution function, using a nonlinear curve-fitting software tool (OriginLab Microcal Northhampton, USA).

2.4 Nanocomposite preparation

Nanocomposites, based on epoxy matrix, were prepared by *in situ* polymerization employing the reactive suspension method [20, 36, 37].

Epoxy resins containing Fe₃O₄ nanoparticles were prepared by the step polymerization of the bisphenol A diglycidyl ether (DGEBA) epoxy monomer with DETA in the presence of Fe₃O₄ synthesized via NHSG process. The formulations were prepared by adding the amine suspension of magnetite nanoparticles (prepared as previously described) in the range between 1 and 8 phr (parts of Fe₃O₄ per hundred parts of resins) of actual Fe₃O₄ content with respect to the epoxy resin.

Composition details and sample codes of the obtained nanocomposites are summarized in Table 2.

Nanocomposite code	DGEBA (g)	DETA (g)	Fe(AcAc) ₃ (g)	Nominal Fe ₃ O ₄ (phr)
Comp-DETA_0	7	0.85	0.00	0
Comp-DETA_1	7	0.85	0.32	1
Comp-DETA_2	7	0.85	0.65	2
Comp-DETA_4	7	0.85	1.29	4
Comp-DETA_8	7	0.85	2.58	8

Table 2: Composition of the thermally-curable nanocomposite formulations [34]

A typical formulation was prepared by mixing magnetite suspension and epoxy monomer by using a magnetic stirrer (15 min mixing time) and an ultrasonic bath (15 min mixing time).

The formulations were casted into silicone moulds having cavities with dimension 8 × 1 × 0.3 cm³. All the formulations were cured at 100-120 °C for 3 h and post-cured at 130-150°C for 30 min.

2.5 Nanocomposite characterization

TEM analysis was carried out on nanocomposite samples in order to evaluate the distribution and dispersion of magnetic nanoparticles into the polymer matrix and correlate the microstructural features with the magnetic functional properties of the nanocomposite. Nanocomposite samples for microscopic analysis were sectioned into ultrathin slices (100-150 nm) at -30 °C using a cryoultramicrotome Leica UC6

(Leica Microsystems, Austria). Sample sections were collected on dimethylsulfoxide-water solution and then deposited on 200 mesh copper grids.

Infra-red spectroscopy (IR) characterization was performed to evaluate the epoxy groups conversion; an Avatar 330 FT-IR Thermo Nicolet spectrometer was used, equipped with a diamond crystal and operating in the ATR mode from 4000 to 500 cm^{-1} (64 scans and resolution of 1 cm^{-1})

2.6 Magnetic measurements

Magnetic hysteresis loops and FC/ZFC curves were measured on two nanocomposite samples using a LOT-Quantum Design SQUID magnetometer operating in the temperature range 2-300 K and in the field range 0 – 7 x 10⁴ Oe. FC/ZFC curves were taken using an applied field $H_{\text{app}} = 30$ Oe and an average heating rate of 6 K/min. The behavior off hysteresis lops in the temperature region around T_V was studied using a narrow temperature step. Samples were positioned on a quartz sample holder whose diamagnetic signal was orders of magnitude lower than the magnetic signal from the nanomaterials.

3. Results

3.1 Structure and morphology of nanoparticles/nanocomposites

XRD patterns of Mag-DETA_x powders are reported in Fig. 1. Independent of the precursor-to-solvent ratio, all synthesized powders are composed by magnetite (JCPDS file 01-075-0449) as crystalline phase. No significant contribution from other iron oxide phases was detected by Raman spectroscopy [36]. In particular the Raman spectrum of nanoparticles, already shown in ref. [36] , exhibits the characteristic bands of magnetite at 668 cm^{-1} assigned to the A_{1g} vibrational mode. The absence of iron oxides different from magnetite is also supported by the high saturation magnetization values (see Table 3).

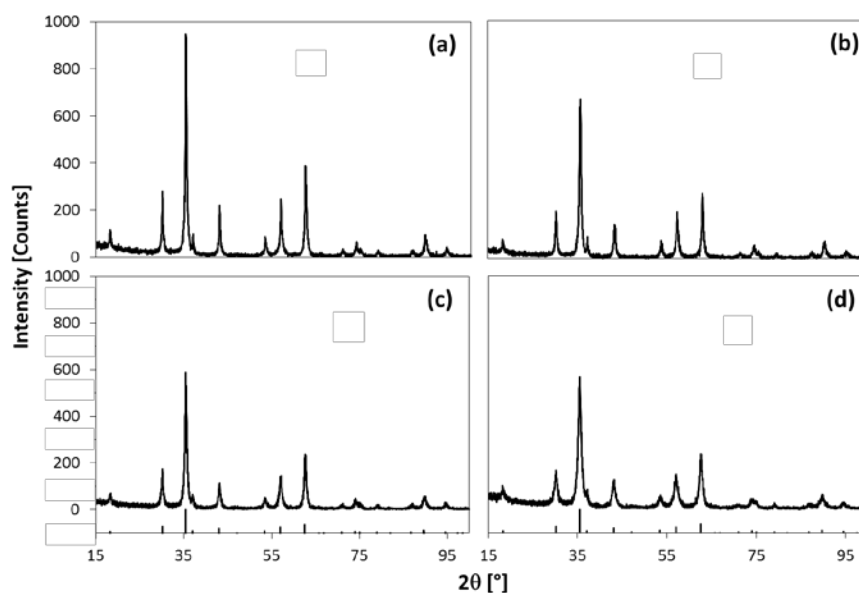


Figure 1: XRD patterns of nanoparticle powders, respectively Mag-DETA_1 (a), Mag-DETA_2 (b), Mag-DETA_4 (c) and Mag-DETA_8 (d) (Magnetite reference pattern is the JCPDS file # 01-075-0449)

TEM images reveal that magnetite particles are nanometer-sized crystals with irregular and anisotropic shapes, such as tetragonal and hexagonal structures (Fig. 2). It can be noted that in addition to nanoparticles with sizes in the 10 nm range, larger nanostructures, between 35 and 70 nm in size, are also present. These larger particles seem to decrease in number and size as the precursor-solvent ratio increases.

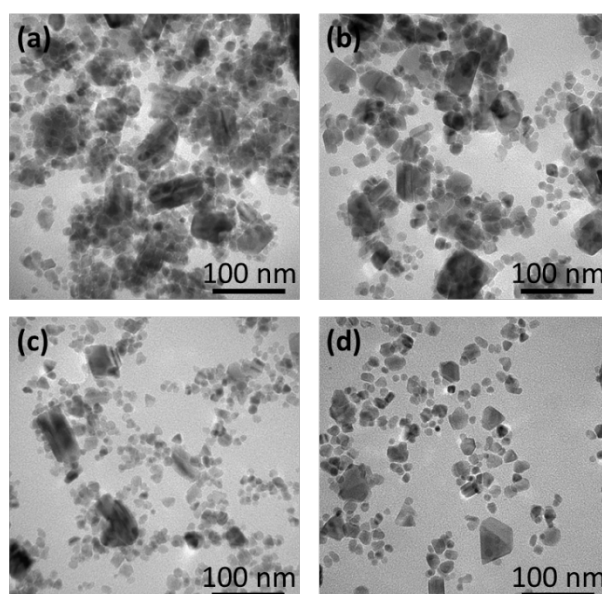
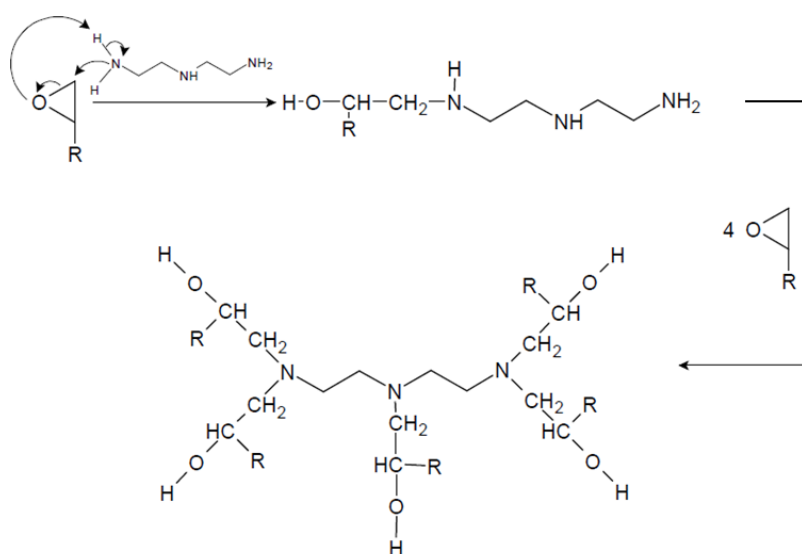


Figure 2: TEM images of Fe_3O_4 nanoparticles, obtained at different precursor-to-solvent ratio: respectively Mag-DETA_1 (a), Mag-DETA_2 (b), Mag-DETA_4 (c) and Mag-DETA_8 (d)

DGEBA monomers can polymerize to form a cross-linked structure via step-growth polymerization by reacting with amines, phenols, mercaptans, isocyanates or acids. Amines are the most commonly used curing agents/hardeners for epoxides and the case of step-growth polymerizations is mainly represented by epoxy-amine reactions, that can be considered the key-reaction in the 'reactive suspension method' for the system Fe_3O_4 -DETA-DGEBA.

In particular, DETA has five reactive sites and the polymerization reaction between DETA and DGEBA can lead to a highly crosslinked 3D network as shown in Scheme 1.



Scheme 1: Reaction mechanism between DETA and DGEBA

The development of the three-dimensional network resulting from polymerization reaction during the nanocomposite preparation was followed by IR spectroscopy. The degree of epoxy groups conversion (determined by FT-IR analysis, according to the decrement of the peak centered at 914 cm^{-1} corresponding to the asymmetric stretching of oxirane ring) is relatively high and almost equal (more than 90%) for all the composite materials, as shown by IR spectra (Fig. 3). This suggests that the ring-opening reaction was not affected by the presence of both the nanoparticles and by-products of the reaction between $\text{Fe}(\text{AcAc})_3$ and DETA.

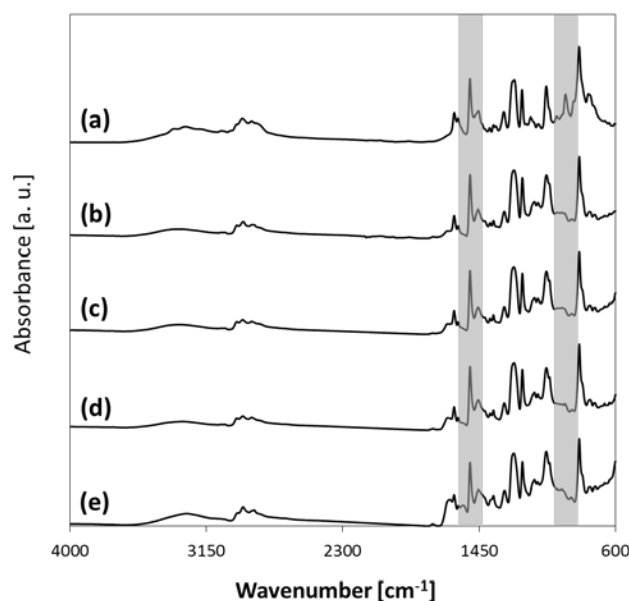


Figure 3: FT-IR spectra of the not cured nanocomposite (a) and cured sample, respectively Comp-DETA_1 (b), Comp-DETA_2 (c), Comp-DETA_4 (d) and Comp-DETA_8 (e)

TEM micrographs of epoxy-magnetite nanocomposites show the presence of a dispersed phase attributable to the magnetite nanoparticles (Fig. 4). Even if some particle agglomeration phenomenon is apparent, a sufficiently homogeneous distribution and dispersion of the filler was reached for the majority of the samples, avoiding the use of any coupling agent and/or time-consuming, complex dispersion treatments for samples preparation.

TEM image analysis has been carried out to get information about the size distribution of nanoparticles embedded in the polymeric matrix. Experimental histograms and fitting curves are shown in Fig. 5. The mean E.C.D. for all samples is reported in Table 3. Histograms for Mag-DETA_1 and Mag-DETA_2 samples are compatible with a bimodal distribution, while samples Mag-DETA_4 and Mag-DETA_8 are characterized by a substantially monomodal distribution with an asymmetry towards larger sizes.

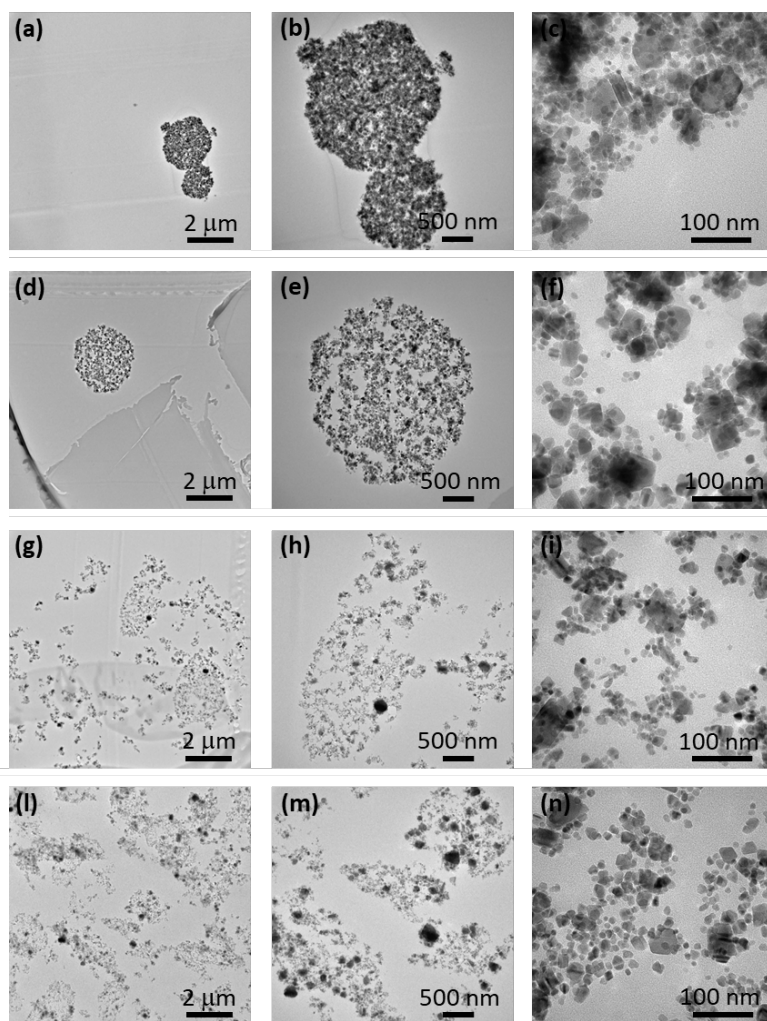


Figure 4: TEM images of Mag-DETA_1 (a-c), Mag-DETA_2 (d-f), Mag-DETA_4 (g-i) and Mag-DETA_8 (l-n) nanocomposites, at increasing magnifications from left to right.

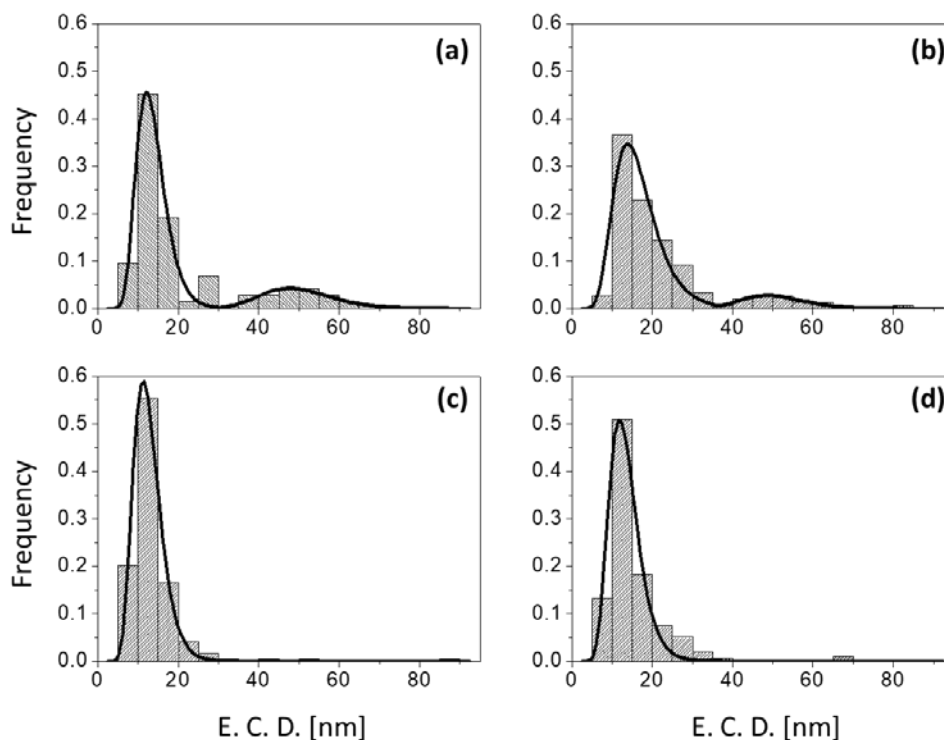


Figure 5: Nanoparticle size distributions obtained by TEM image analysis: (a) Mag-DETA_1, (b) Mag-DETA_2, (c) Mag-DETA_4 and (d) Mag-DETA_8.

3.2 Magnetic properties

The room-temperature saturation magnetization of all nanopowders (obtained by fitting the high-field region of the $M(H)$ curves to the standard approach to saturation curve for a ferri/ferromagnetic material [38]) are given in Table 3. The measured values are in the range 55-61 emu/g, in good agreement with typical results for magnetite nanoparticles of similar size [20, 39]. The reduction with respect to the bulk value has been related to the presence of a magnetically “dead” layer at the nanoparticle surface [17, 18].

The magnetic properties of two representative nanocomposite samples (Mag-DETA_2, Mag-DETA_8) have been investigated. The choice of samples was suggested by the nanoparticle distributions as reported in Fig. 5 and Table 3: sample Mag-DETA_2 displays a bimodal size distribution and a greater mean size of the small particles, whereas nanoparticles embedded in sample Mag-DETA_8 have a basically monomodal distribution and a lower mean size. The room temperature saturation magnetization of these nanocomposites is given in Table 4.

Sample (powder) Mag-DETA_x	Powders M_s (emu/g)	Nanocomposite Comp-DETA_n	Mean E.C.D Peak 1 [nm]	Mean E.C.D. Peak 2 [nm]
x=1	58.1	n=1	14±4	50±9
x=2	60.9	n=2	17±6	51±8
x=4	55.3	n=4	13±4	/
x=8	58.1	n=8	13±4	/

Table 3: Saturation magnetization of nanopowders and mean nanoparticle sizes corresponding to the first and the second peak (if applicable) of the equivalent circular diameter distribution of all nanocomposites

Nanocomposite Comp-DETA_n	Nanocomposites M_s (emu/g)	x	T_v (K) from ZFC curve	T_m from p(T_v) curve	$\langle T_v \rangle$ (K) from p(T_v) curve
n=2	0.86	0.0141	113.0	113.2	110.5
n=8	8.77	0.1509	111.0	110.2	109.4

Table 4: Magnetic and structural data of two nanocomposite samples: saturation magnetization; magnetic volume fraction; mean Verwey-transition temperature estimated from the inflection point of the ZFC curve; mode and mean value of the Verwey-temperature distribution.

The FC/ZFC curves of nanocomposites Comp-DETA_n (n=2,8), normalized to the room-temperature value, are shown in Fig. 6.

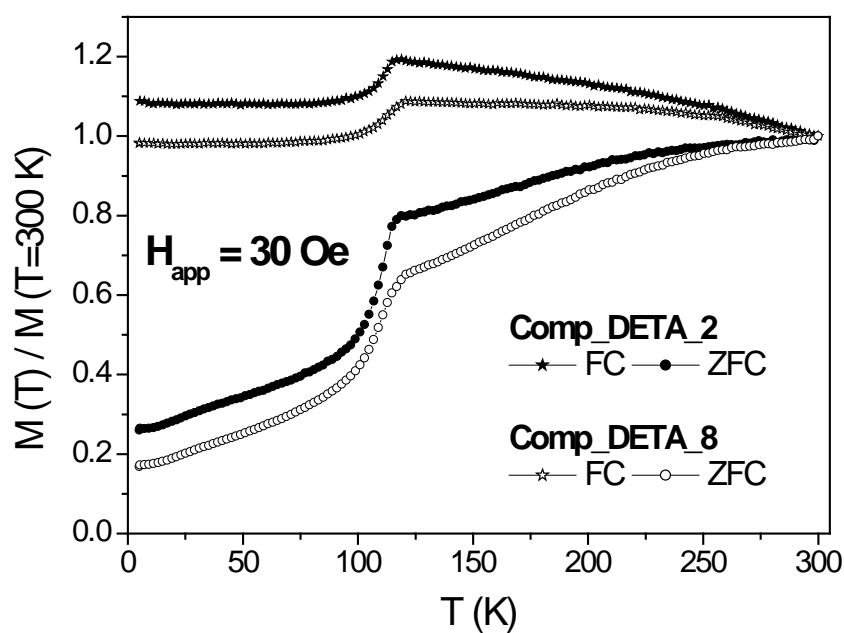


Figure 6: FC/ZFC curves (normalized to the room-temperature values) of the studied magnetite nanocomposites.

The absence of a definite peak in the ZFC curve, the occurrence of a rather flat FC curve and a merging temperature coincident with room temperature are typical hallmarks of nanoparticles blocked over the whole measured temperature range, either because of their size [40] or because of interactions [17, 37, 41, 42]; however, both FC and ZFC curves exhibit a marked upward step on heating just below $T = 120$ K, clearly related to the Verwey transition. T_V can be estimated from the inflexion point of the ZFC curves; the resulting values are reported in Table 3 (the same results are obtained from the FC curves). It should be noted that $T_V = 123$ K in high-quality, bulk magnetite crystals [30, 43]. Considering the experimental relationship between the observation of T_V in nanometer-sized magnetite and the high quality of the sample [30], it can be concluded that a fraction of rather high quality magnetite crystals is present in our systems, in agreement with TEM images (Fig. 4).

Magnetic hysteresis loops of the two samples, measured above and below T_V (at $T = 75$ K and 150 K, respectively) are reported in Fig. 7 (top panels). The most distinctive features observed on heating from below to above T_V are a strong reduction of the coercive field H_C associated with a corresponding increase in the slope of loops (dM/dH). Full hysteresis loops (from $H_{min} = -70$ kOe to $H_{max} = +70$ kOe) at room temperature are shown in Fig. 7 (bottom panel). When the reduced magnetization M/M_s is plotted, the loops are almost superimposed. In both samples, a clearly non-saturating behavior of the magnetization is observed up to field values as large as 70 kOe. This behaviour indicates that a fraction of particles is in the superparamagnetic state at room temperature. In fact, using the typical value of the cubic anisotropy of magnetite around room temperature ($K_1 \cong 1.3 \times 10^5$ erg/cm³ [44]) and taking into account the particle size distributions of Fig. 5, the blocking temperature of the smaller particles in the distribution is estimated to be well below room temperature.

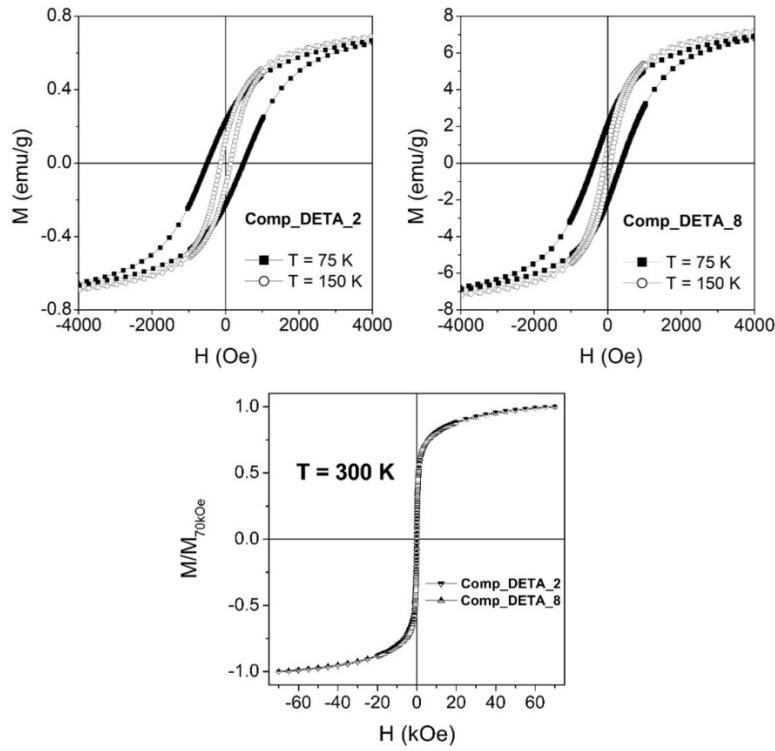


Figure 7: Top panels: hysteresis loops in the low-field region above and below the Verwey transition in the studied nanocomposites. Bottom panel: hysteresis loops in the interval $-70 \text{ kOe} \leq H \leq 70 \text{ kOe}$ at $T = 300 \text{ K}$

The hysteresis loop parameters have been investigated with special attention to the critical region around $\langle T_V \rangle$, and are summarized in Fig. 8. The high-field magnetization M_{HF} ($H_{app} = 70 \text{ kOe}$) is shown in panel (a): no particular change of M_{HF} is observed around $\langle T_V \rangle$. The different magnetic signal from the two samples is related to the different content of magnetite in the polymeric matrix (the magnetic volume fraction x in these samples is estimated from the data of Table 2 and is reported in Table 4).

On the contrary, the coercive field H_c exhibits a sharp decrease on heating from 95 K to about 120 K (see Fig. 8b). Such a behavior is clearly related to the Verwey transition, although it is definitely less sharp and less strong than in bulk magnetite single crystals [45]; the effect we measure around $\langle T_V \rangle$ is more apparent in sample Comp-DETA_2 than in sample Comp-DETA_8. Outside this region, the measured $H_c(T)$ curve exhibits features typical of the coercive field of an assembly of polydisperse magnetic nanoparticles which undergo blocking over an extended range of temperatures, typically resulting in smooth, continuous decrease of H_c with increasing measurement temperature [46]. It should be noted that a nonzero coercive field is measured even at room temperature in both samples, in agreement with the presence of large particles which are still blocked there; however, H_c is definitely lower in sample Comp-DETA_8, which contains a higher fraction of smaller particles which are in the superparamagnetic state at 300 K (see Figure 7).

A quite complementary behavior is observed on the maximum magnetic susceptibility of the loop $\chi_{Max} = (dM/dH)_{Max}$ (Fig. 8c). In sample Comp-DETA_2, this quantity is almost constant both above and below the

Verwey temperature region, while it almost doubles on heating from 95 to 120 K. A similar, though slightly less sharp effect is observed in sample Comp-DETA_8, where χ_{Max} exhibits some change even outside this region.

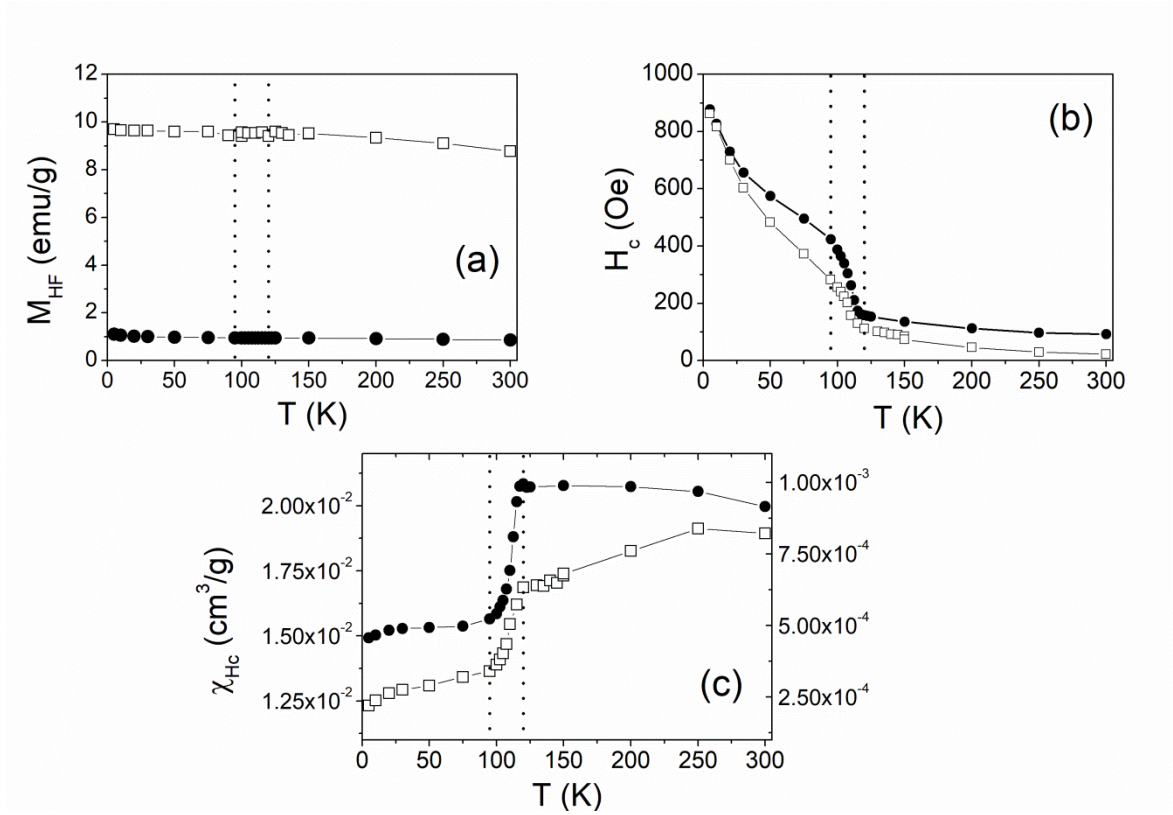


Figure 8: Temperature behavior of high-field magnetization M_{HF} (panel [a]); coercive field H_c (panel [b]); maximum magnetic susceptibility χ_{Max} (panel [c]) in samples Comp-DETA_2 (full symbols) and Comp-DETA_8 (open symbols).

Vertical dotted lines indicate $T = 95$ K and $T = 120$ K.

Valuable information about the distribution of Verwey temperatures in our samples can be obtained by plotting χ_{Max} as a function of the reciprocal of the coercive field H_c in a temperature region around T_v , as shown in Fig. 9. The limits of the investigated temperature interval were taken at $T = 95$ K and $T = 120$ K, i.e., just before and after the jumps of H_c and χ_{Max} (Fig. 8 b,c).

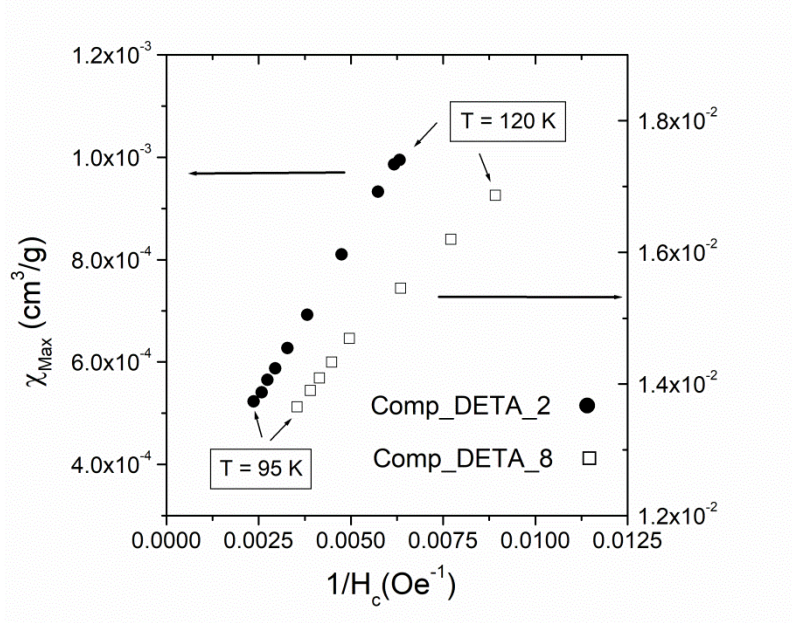


Figure 9: Maximum magnetic susceptibility plotted as a function of H_c^{-1} around $\langle T_V \rangle$ (see text for details).

In fact, a functional relationship between maximum susceptibility and coercive field of the type:

$$\chi_{Max} = \alpha \frac{M_s}{H_c} \quad (1)$$

is expected in systems where the magnetization process occurs by coherent rotation of the magnetization vector away from the easy axis by effect of an applied field [38]. The same condition applies to single-domain, blocked nanoparticles also (Stoner-Wohlfarth model). In Equation (1), M_s is the intrinsic magnetization of nanoparticles (see Table 2) and α is a numeric proportionality constant which depends on the value and symmetry of the crystal anisotropy [38].

The magnetite nanoparticles embedded in these nanocomposites can be considered as being predominantly in the single-domain state, the crossover between single and multiple domain configuration being estimated by different theoretical calculations to occur around 60 - 80 nm in magnetite particles [47–49]. Comparison with the histograms reported in Fig. 5 reveals that basically all particles are single-domain in sample Comp-DETA_8, whereas a very small fraction of multiple-domain nanoparticles could be present in sample Comp-DETA_2. In the following, the contribution from multiple-domain particles, if any, will be neglected.

In the region of interest, the single-domain nanoparticles contained in the two samples can be either in the magnetically blocked or in the superparamagnetic state. The shape of the FC/ZFC curves (Fig. 6) clearly indicates that in both samples the average blocking temperature is above room temperature; **however, a fraction of superparamagnetic particles exists at room temperature, as indicated by the non-saturating behaviour of the high-field magnetization (Figure 7); in addition, the presence of a superparamagnetic**

fraction at even lower temperatures, and specifically around T_V , cannot be excluded because of the considerable polydispersity of these systems. In principle, therefore, one should separately consider both types of nanoparticles (i.e., blocked and superparamagnetic) when the region around T_V is studied.

As known, above the Verwey transition the magnetic anisotropy has cubic symmetry, with easy axes corresponding to the $\langle 111 \rangle$ directions of the cubic cell (the anisotropy constant K_1 being negative at high temperature), while below T_V the magnetic anisotropy becomes uniaxial with easy axis corresponding to the c-axis of the monoclinic cell [50, 51]. These changes of symmetry have basically no influence on the small fraction of particles which possibly are in the superparamagnetic state around T_V : the temperature behavior of the magnetic anisotropy constants below and above T_V [44, 51] clearly indicates that a particle already in the superparamagnetic state below T_V remains in this state above T_V .

As a consequence, we assume that the contribution of superparamagnetic particles to the measured magnetic properties remains basically the same over the narrow interval under consideration ($T = 95$ K to $T = 120$ K), playing no substantial role in the observed jumps of both χ_{Max} and H_c , which must be entirely ascribed to effects taking place in the magnetically blocked particles only.

In a system of blocked, single-domain nanoparticles with uniaxial anisotropy K_u and randomly distributed easy directions, the predictions of the Stoner-Wohlfarth model [38] apply:

$$\begin{aligned} H_c &\cong 0.96 \frac{K_u}{M_s} \\ \chi_{Max} &\cong 0.56 \frac{M_s^2}{K_u} \end{aligned} \quad (2)$$

Therefore, in the uniaxial case the α coefficient of Eq. (1) is easily calculated to be $\alpha_u = 0.55$. On the contrary, in a system of blocked single-domain nanoparticles with negative cubic anisotropy ($K_1 < 0$) and randomly distributed easy directions, the following predictions [52] apply:

$$\begin{aligned} H_c &\cong 0.37 \frac{|K_1|}{M_s} \\ \chi_{Max} &\cong 8.00 \frac{M_s^2}{|K_1|} \end{aligned} \quad (3)$$

resulting in a much higher α coefficient ($\alpha_c = 2.96$). The difference between α_u and α_c is deemed responsible for the difference observed in both samples between the values taken at $T = 95$ K and the ones taken at $T = 120$ K (Fig. 9). In fact, in this narrow temperature interval, the saturation magnetization can be considered as a constant (see Fig. 8a).

In the interval 95-120 K, the value of χ_{Max} steadily increases with increasing H_c^{-1} , following an almost linear law, as clearly observed in Fig. 9. Such an effect can be explained by supposing that the Verwey transition does not occur at the same temperature in all magnetite particles of the studied nanocomposites. If one

considers that the fraction of nanoparticles exhibiting cubic anisotropy (f_c) is equal to zero at $T = 95$ K and equal to one at $T = 120$ K, the monotonic increase of χ_{Max} with H_c^{-1} is easily associated to the growth of the transformed cubic-anisotropy fraction f_c from 0 to 1. The growth curve $f_c(T)$ is obtained assuming a linear relationship between the values of χ_{Max} at each temperature in the interval 95-120 K and the value of f_c at the same temperature, leading to the expression:

$$f_c(T) = \frac{\chi_{Max}(T) - \chi_{Max}(95\text{ K})}{\chi_{Max}(120\text{ K}) - \chi_{Max}(95\text{ K})} \quad (4)$$

This growth curve turns out to be S-shaped and is shown in Fig. 10 (top panel) for both samples. The full lines are Richards curves (generalized logistic curves) which appear to accurately fit the experimental data.

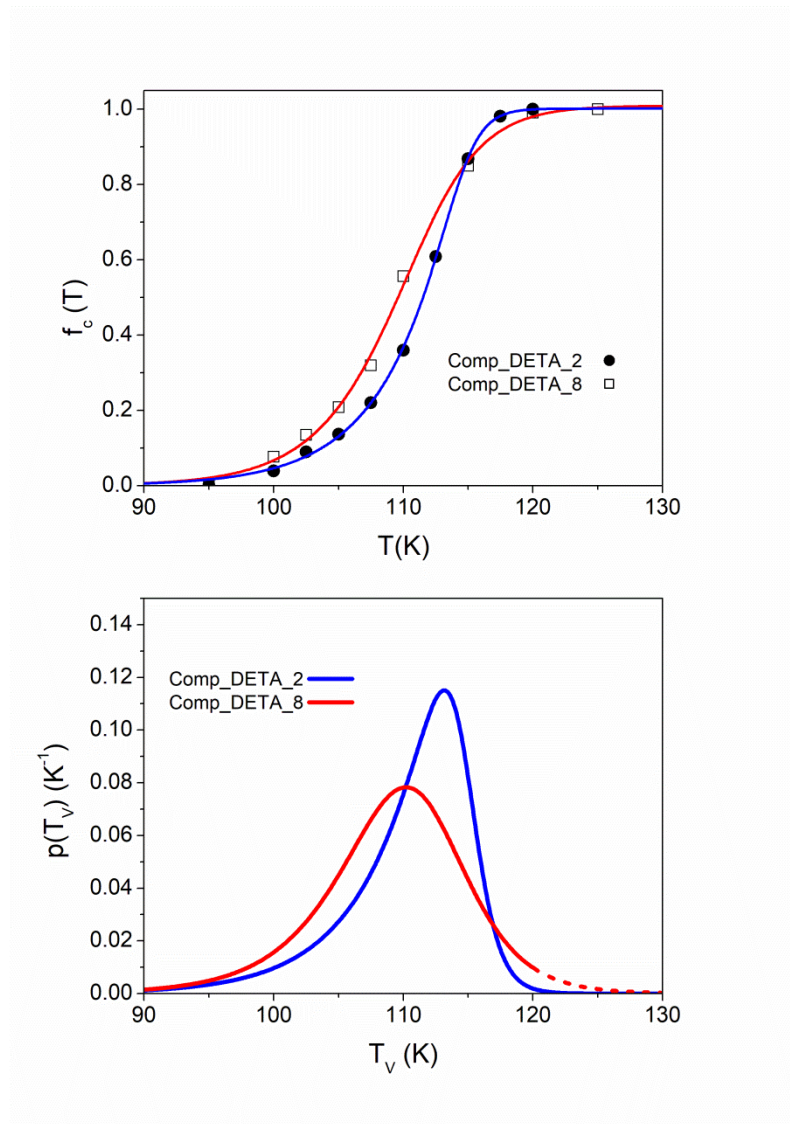


Figure 10: Top Panel: transformed cubic-anisotropy fraction f_c as a function of measurement temperature for both nanocomposite samples (symbols: data obtained from Eq. (4); lines: fitting Richards growth curves). Bottom panel: normalized Verwey-temperature distribution function $p(T_v)$ for both samples.

In sample Comp-DETA_8, characterized by a monomodal particle distribution and a lower mean particle size, a larger transformed fraction is observed at all temperatures below 115 K.

The derivative with respect to temperature of each fitting curve of Fig 10 (top panel) gives the elementary transformed fraction in the temperature interval between T and $T+dT$; this corresponds to the fraction of particles which undergo the Verwey transition in the same temperature interval, i.e., whose Verwey transition temperature is between T and $T+dT$. As a consequence, the derivative of each fitting curve with respect to temperature, is proportional to the actual distribution of the Verwey transition temperatures $p(T_V)$ present in either sample $\left(p(T_V) \propto \frac{df_c}{dT}\bigg|_{T=T_V}\right)$. The resulting normalized $p(T_V)$ curves are shown in Fig. 10 (bottom panel). It should be noted that the fitting function proposed to represent $f_c(T)$ is not fully accurate in Comp-DETA_8, resulting in a rather unphysical tail of the $p(T_V)$ curve above $T = 120$ K (dashed line) which should therefore be discarded. The mode of the distribution is at $T_m = 113.2$ K and $T_m = 112.2$ K, and the mean value is $\langle T_V \rangle = 110.5$ K and $\langle T_V \rangle = 109.4$ K in samples Comp-DETA_2 and Comp-DETA_8, respectively. The agreement between the values estimated from the inflection points of ZFC curves and the ones obtained by the present analysis (particularly with the modal temperatures T_m) is striking. It should be explicitly reminded that ZFC curves represent the magnetic response of a demagnetized sample submitted to a very small field, whereas χ_{Max} and H_c are quantities measured on a major hysteresis loop. The agreement between the T_V values estimated analyzing very different magnetic states of a sample strengthens the proposed procedure of analysis.

Finally, an estimate of the uniaxial anisotropy constant K_u of the studied nanoparticles at low temperature ($T = 5$ K) is obtained from the value of the coercive field (Fig. 8b). Inserting in Eq. (2) $H_c(T=5 \text{ K}) \cong 878/862$ Oe, $M_s \cong 321/392 \text{ emu/cm}^3$ (taken from the values measured on nanopowders (Table 2) extrapolated to $T = 5$ K) one gets $K_u \cong 2.94 \times 10^5 / 3.51 \times 10^5 \text{ erg/cm}^3$ in samples Comp-DETA_2/8, respectively. Both values are slightly higher than the low-temperature K_u of bulk monoclinic magnetite ($K_u = 2.1 \times 10^5 \text{ emu/cm}^3$) [44]; this is a general behavior, usually related to surface effects [20]; in the present case, the difference between the two estimates is compatible with the lower mean nanoparticle size in sample Comp-DETA_8 with respect to sample Comp-DETA_2.

4. Conclusion

Significant changes of magnetic properties connected to the Verwey transition have been observed in two nanocomposite polymeric materials containing polydisperse magnetite particles. Such particles were synthesized starting from the same precursors through the same chemical route, but are characterized by different size distributions and mean sizes. In both investigated materials, the transition takes place over a temperature interval of about 15 K and the average Verwey-transition temperature is slightly below the

value attributed to high-quality, bulk magnetite. A detailed study of the region around $\langle T_V \rangle$ indicates that the changes of the maximum magnetic susceptibility and of the coercive field are ascribed to blocked nanoparticles only, whereas small particles which are expected to be in the superparamagnetic state do not play any important role. In blocked particles, the transition from uniaxial to cubic magnetic anisotropy takes place gradually over the temperature interval from $T = 95$ K to $T = 120$ K. This behavior indicates a continuous distribution of Verwey temperatures described by the function $p(T_V)$ which has been directly obtained from the magnetic analysis. The existence of a distribution of Verwey-transition temperatures is almost certainly related to the polydispersity of the investigated nanoparticle systems; however, it is not possible to directly link the $p(T_V)$ function to the actual distribution of nanoparticle sizes in the absence of more precise information about the role of particle size on the value of the Verwey transition temperature and of the physical mechanisms (related to, e.g., stoichiometry, particle shape, surface, defectiveness) which influence the transition in nanometer-sized magnetite.

Competing interests

The authors have no competing interests to declare

Funding

This research did not receive any specific grant from funding agencies in the public, commercial, or not-for-profit sectors.

References

1. Walz F (2002) The Verwey transition - a topical review. *J Phys Condens Matter* 14:R285–R340. <https://doi.org/10.1088/0953-8984/14/12/203>
2. García J, Subías G (2004) The Verwey transition - A new perspective. *J Phys Condens Matter* 16:. <https://doi.org/10.1088/0953-8984/16/7/R01>
3. Tsuya N, Arai KI, Ohmori K (1977) Effect of magnetoelastic coupling on the anisotropy of magnetite below the transition temperature. *Phys B+C* 86–88:959–960. [https://doi.org/10.1016/0378-4363\(77\)90759-8](https://doi.org/10.1016/0378-4363(77)90759-8)
4. Tartaj P, Morales P, Veintemillas-verdaguer S, Gonz T (2003) The preparation of magnetic nanoparticles for applications in biomedicine. *J Phys D Appl Phys* 36:R182–R197
5. Sun S, Zeng H, Robinson DB, et al (2004) Monodisperse MFe_2O_4 ($M = Fe, Co, Mn$) Nanoparticles. *J Am Chem Soc* 126:273–279. <https://doi.org/10.1021/JA0380852>

6. Pinna N, Grancharov S, Beato P, et al (2005) Magnetite Nanocrystals: Nonaqueous Synthesis, Characterization, and Solubility. *Chem Mater* 17:3044–3049. <https://doi.org/10.1021/CM050060+>
7. Chaichi M, Sharif F, Mazinani S (2017) Preparation and evaluation of magnetic field-induced orientation on magnetic nanoparticles on PVA nanocomposite films. *J Mater Sci* 53:5051–5062. <https://doi.org/10.1007/s10853-017-1923-7>
8. Li J, Chen Y, Wu Q, et al (2018) Synthesis of sea-urchin-like Fe₃O₄/SnO₂ heterostructures and its application for environmental remediation by removal of p-chlorophenol. *J Mater Sci*. <https://doi.org/10.1007/s10853-018-2899-7>
9. Jalil WBF, Pentón-Madrigal A, Mello A, et al (2017) Low toxicity superparamagnetic magnetite nanoparticles: One-pot facile green synthesis for biological applications. *Mater Sci Eng C* 78:457–466. <https://doi.org/10.1016/j.msec.2017.04.066>
10. Sen T, Shimpi NG, Mishra S, Sharma R (2014) Polyaniline/ γ -Fe₂O₃ nanocomposite for room temperature LPG sensing. *Sensors Actuators, B Chem* 190:120–126. <https://doi.org/10.1016/j.snb.2013.07.091>
11. Loh KS, Lee YH, Musa A, et al (2008) Use of Fe₃O₄ nanoparticles for enhancement of biosensor response to the herbicide 2,4-dichlorophenoxyacetic acid. *Sensors* 8:5775–5791. <https://doi.org/10.3390/s8095775>
12. Mohammed L, Gomaa HG, Ragab D, Zhu J (2017) Magnetic nanoparticles for environmental and biomedical applications: A review. *Particuology* 30:1–14. <https://doi.org/10.1016/j.partic.2016.06.001>
13. Ghazanfari MR, Kashefi M, Shams SF, Jaafari MR (2016) Perspective of Fe₃O₄ Nanoparticles Role in Biomedical Applications. *Biochem Res Int* 2016:1–32. <https://doi.org/10.1155/2016/7840161>
14. Sarkar S, Guibal E, Quignard F, SenGupta AK (2012) Polymer-supported metals and metal oxide nanoparticles: Synthesis, characterization, and applications. *J Nanoparticle Res* 14:. <https://doi.org/10.1007/s11051-011-0715-2>
15. Pang J, Li Z, Li S, et al (2018) Folate-conjugated zein/Fe₃O₄ nanocomplexes for the enhancement of cellular uptake and cytotoxicity of gefitinib. *J Mater Sci* 53:14907–14921. <https://doi.org/10.1007/s10853-018-2684-7>
16. Kim KJ, Park JW (2017) Stability and reusability of amine-functionalized magnetic-cored dendrimer for heavy metal adsorption. *J Mater Sci* 52:843–857. <https://doi.org/10.1007/s10853-016-0380-z>

17. Caruntu D, Caruntu G, O'Connor CJ (2007) Magnetic properties of variable-sized Fe₃O₄ nanoparticles synthesized from non-aqueous homogeneous solutions of polyols. *J Phys D Appl Phys* 40:5801–5809. <https://doi.org/10.1088/0022-3727/40/19/001>
18. Sciancalepore C, Gualtieri AF, Scardi P, et al (2018) Structural characterization and functional correlation of Fe₃O₄ nanocrystals obtained using 2-ethyl-1,3-hexanediol as innovative reactive solvent in non-hydrolytic sol-gel synthesis. *Mater Chem Phys* 207:337–349. <https://doi.org/10.1016/j.matchemphys.2017.12.089>
19. Knobel M, Nunes WC, Socolovsky LM, et al (2008) Superparamagnetism and Other Magnetic Features in Granular Materials: A Review on Ideal and Real Systems. *J Nanosci Nanotechnol* 8:2836–2857. <https://doi.org/10.1166/jnn.2008.15348>
20. Sciancalepore C, Bondioli F, Messori M, et al (2015) Epoxy nanocomposites functionalized with in situ generated magnetite nanocrystals: Microstructure, magnetic properties, interaction among magnetic particles. *Polym (United Kingdom)* 59:278–289. <https://doi.org/10.1016/j.polymer.2014.12.047>
21. López Maldonado KL, De La Presa P, Flores Tavizón E, et al (2013) Magnetic susceptibility studies of the spin-glass and Verwey transitions in magnetite nanoparticles. *J Appl Phys* 113:2013–2016. <https://doi.org/10.1063/1.4797628>
22. Markovich G, Fried T, Poddar P, et al (2002) Observation of the Verwey Transition in Fe₃O₄ Nanocrystals. *MRS Proc* 746:Q4.1. <https://doi.org/10.1557/PROC-746-Q4.1>
23. Goya GF, Berquó TS, Fonseca FC, Morales MP (2003) Static and dynamic magnetic properties of spherical magnetite nanoparticles. *J Appl Phys* 94:3520–3528. <https://doi.org/10.1063/1.1599959>
24. Hevroni A, Bapna M, Piotrowski S, et al (2016) Tracking the Verwey Transition in Single Magnetite Nanocrystals by Variable-Temperature Scanning Tunneling Microscopy. *J Phys Chem Lett* 7:1661–1666. <https://doi.org/10.1021/acs.jpcllett.6b00644>
25. Arelaro AD, Brandl AL, Lima E, et al (2005) Interparticle interactions and surface contribution to the effective anisotropy in biocompatible iron oxide nanoparticles used for contrast agents. *J Appl Phys* 97:2003–2006. <https://doi.org/10.1063/1.1853931>
26. Wang J, Chen Q, Li X, et al (2004) Disappearing of the Verwey transition in magnetite nanoparticles synthesized under a magnetic field: Implications for the origin of charge ordering. *Chem Phys Lett* 390:55–58. <https://doi.org/10.1016/j.cpllett.2004.04.005>

27. Lee J, Kwon SG, Park J-G, Hyeon T (2015) Size Dependence of Metal–Insulator Transition in Stoichiometric Fe₃O₄ Nanocrystals. *Nano Lett* 15:4337–4342. <https://doi.org/10.1021/acs.nanolett.5b00331>
28. Mitra A, Mohapatra J, Meena SS, et al (2014) Verwey Transition in Ultrasmall-Sized Octahedral Fe₃O₄ Nanoparticles. *J Phys Chem C* 118:19356–19362. <https://doi.org/10.1021/jp501652e>
29. Shepherd JP, Koenitzer JW, Aragón R, et al (1991) Heat capacity and entropy of nonstoichiometric magnetite Fe_{3(1-δ)}O₄: The thermodynamic nature of the Verwey transition. *Phys Rev B* 43:8461. <https://doi.org/10.1103/PhysRevB.43.8461>
30. Schmitz-Antoniak C, Schmitz D, Warland A, et al (2016) Reversed ageing of Fe₃O₄ nanoparticles by hydrogen plasma. *Sci Rep* 6:2–7. <https://doi.org/10.1038/srep20897>
31. Sangermano M, Allia P, Tiberto P, et al (2013) Photo-cured epoxy networks functionalized with Fe₃O₄ generated by non-hydrolytic sol-gel process. *Macromol Chem Phys* 214:508–516. <https://doi.org/10.1002/macp.201200494>
32. Niederberger M, Pinna N (2009) Metal Oxide Nanoparticles in Organic Solvents Synthesis, Formation, Assembly and Application. Springer
33. Sciancalepore C, Rosa R, Barrera G, et al (2014) Microwave-assisted nonaqueous sol-gel synthesis of highly crystalline magnetite nanocrystals. *Mater Chem Phys* 148:117–124
34. Sciancalepore C, Bondioli F, Manfredini T, Gualtieri A (2015) Quantitative phase analysis and microstructure characterization of magnetite nanocrystals obtained by microwave assisted non-hydrolytic sol-gel synthesis. *Mater Charact* 100:88–97. <https://doi.org/10.1016/j.matchar.2014.12.013>
35. Xu R, Di Guida OA (2003) Comparison of sizing small particles using different technologies. *Powder Technol* 132:145–153. [https://doi.org/10.1016/S0032-5910\(03\)00048-2](https://doi.org/10.1016/S0032-5910(03)00048-2)
36. Sciancalepore C, Bondioli F, Messori M (2017) Non-hydrolytic sol–gel synthesis and reactive suspension method: an innovative approach to obtain magnetite–epoxy nanocomposite materials. *J Sol-Gel Sci Technol* 81:69–83. <https://doi.org/10.1007/s10971-016-4095-z>
37. Barrera G, Sciancalepore C, Messori M, et al (2017) Magnetite-epoxy nanocomposites obtained by the reactive suspension method: Microstructural, thermo-mechanical and magnetic properties. *Eur Polym J* 94:354–365. <https://doi.org/10.1016/j.eurpolymj.2017.07.022>
38. Chikazumi S (1997) Physics of Ferromagnetism. Oxford University Press

39. Lin C-R, Chiang R-K, Wang J-S, Sung T-W (2006) Magnetic properties of monodisperse iron oxide nanoparticles. *J Appl Phys* 99:08N710. <https://doi.org/10.1063/1.2172891>
40. Allia P, Barrera G, Tiberto P (2018) Linearized rate-equation approach for double-well systems: Cooling- and temperature-dependent low-field magnetization of magnetic nanoparticles. *Phys Rev B* 98:134423. <https://doi.org/10.1103/PhysRevB.98.134423>
41. Uva M, Mencuccini L, Atrei A, et al (2015) On the Mechanism of Drug Release from Polysaccharide Hydrogels Cross-Linked with Magnetite Nanoparticles by Applying Alternating Magnetic Fields: the Case of DOXO Delivery. *Gels* 1:24–43. <https://doi.org/10.3390/gels1010024>
42. Ningthoujam RS, Vatsa RK, Prajapat CL, et al (2010) Interaction between amorphous ferromagnetic Co-Fe-B particles in conducting silver matrix prepared by chemical reduction route. *J Alloys Compd* 492:40–43. <https://doi.org/10.1016/j.jallcom.2009.11.119>
43. Craco L, Laad MS, Müller-Hartmann E (2006) Verwey transition in Fe_3O_4 investigated using LDA+DMFT. *Phys Rev B* 74:064425. <https://doi.org/10.1103/PhysRevB.74.064425>
44. Abe K, Miyamoto Y, Chikazumi S (1976) Magnetocrystalline Anisotropy of Low Temperature Phase of Magnetite. *J. Phys. Soc. Japan* 41:1894–1902
45. Özdemir Ö (2000) Coercive force of single crystals of magnetite at low temperatures. *Geophys J Int* 141:351–356. <https://doi.org/10.1046/j.1365-246X.2000.00081.x>
46. Mercante LA, Melo WWM, Granada M, et al (2012) Magnetic properties of nanoscale crystalline maghemite obtained by a new synthetic route. *J Magn Magn Mater* 324:3029–3033. <https://doi.org/10.1016/j.jmmm.2012.04.049>
47. Moskowitz BM, Banerjee SK (1979) Grain Size Limits for Pseudosingle Domain Behavior in Magnetite: Implications for Paleomagnetism. *IEEE Trans Magn* 15:1241–1246. <https://doi.org/10.1109/TMAG.1979.1060319>
48. Argyle KS, Dunlop DJ (1984) Theoretical domain structure in multidomain magnetite particles. *Geophys Res Lett* 11:185–188
49. Kirschvink JL, Lowenstam HA (1979) Mineralization and magnetization of chiton teeth: paleomagnetic, sedimentologic, and biologic implications of organic magnetite. *Earth Planet Sci Lett* 44:193–204. [https://doi.org/10.1016/0012-821X\(79\)90168-7](https://doi.org/10.1016/0012-821X(79)90168-7)
50. Kakol Z, Honig JM (1989) Influence of deviations from ideal stoichiometry on the anisotropy parameters of magnetite $\text{Fe}_{3(1-x)}\text{O}_4$. *Phys Rev B* 40:9090–9097.

<https://doi.org/10.1103/PhysRevB.40.9090>

51. Reznicek R, Chlan V, Stepankova H, et al (1983) Magnetocrystalline anisotropy of magnetite. J Magn Magn Mater 31–34:813–814. [https://doi.org/10.1016/0304-8853\(83\)90698-4](https://doi.org/10.1016/0304-8853(83)90698-4)
52. Usov NA, Peschany SE (1997) Theoretical hysteresis loops for single-domain particles with cubic anisotropy. J Magn Magn Mater 174:247–260. [https://doi.org/10.1016/S0304-8853\(97\)00180-7](https://doi.org/10.1016/S0304-8853(97)00180-7)